BNL-213731-2020-JAAM

Boosting CO2 reduction on Fe-N-C with sulfur incorporation: Synergistic electronic and structural engineering

F. Pan, S. Hwang

To be published in "Nano Energy"

February 2020

Center for Functional Nanomaterials

Brookhaven National Laboratory

U.S. Department of Energy

USDOE Office of Science (SC), Basic Energy Sciences (BES) (SC-22)

Notice: This manuscript has been authored by employees of Brookhaven Science Associates, LLC under Contract No. DE-SC0012704 with the U.S. Department of Energy. The publisher by accepting the manuscript for publication acknowledges that the United States Government retains a non-exclusive, paid-up, irrevocable, world-wide license to publish or reproduce the published form of this manuscript, or allow others to do so, for United States Government purposes.

DISCLAIMER

This report was prepared as an account of work sponsored by an agency of the United States Government. Neither the United States Government nor any agency thereof, nor any of their employees, nor any of their contractors, subcontractors, or their employees, makes any warranty, express or implied, or assumes any legal liability or responsibility for the accuracy, completeness, or any third party's use or the results of such use of any information, apparatus, product, or process disclosed, or represents that its use would not infringe privately owned rights. Reference herein to any specific commercial product, process, or service by trade name, trademark, manufacturer, or otherwise, does not necessarily constitute or imply its endorsement, recommendation, or favoring by the United States Government or any agency thereof or its contractors or subcontractors. The views and opinions of authors expressed herein do not necessarily state or reflect those of the United States Government or any agency thereof.

Boosting CO_2 Reduction on Fe-N-C with Sulfur Incorporation: Synergistic Electronic and Structural Engineering

Fuping Pan[a], Boyang Li[b], Erik Sarnello[c], Sooyeon Hwang[d], Yang Gang[a], Xuhui Feng[a], Nadia Mohd Adli[e], Tao Li[c,f], Dong Su[d], Gang Wu[e*], Guofeng Wang[b*], and Ying Li[a*]

[a] J. Mike Walker '66 Department of Mechanical Engineering, Texas A&M University, College Station, Texas 77843, United States

[b] Department of Mechanical Engineering and Materials Science, University of Pittsburgh, Pittsburgh, Pennsylvania 15261, United States

[c] Department of Chemistry and Biochemistry, Northern Illinois University, DeKalb, Illinois 60115, United States

[d] Center for Functional Nanomaterials, Brookhaven National Laboratory, Upton, New York 11973, United States

[e] Department of Chemical and Biological Engineering, University at Buffalo, The State University of New York, Buffalo, New York 14260, United States

[f] Chemistry and Material Science Group, X-ray Science Division, Argonne National Laboratory, Lemont, Illinois 60439, United States

* Corresponding Authors:

Gang Wu (gangwu@buffalo.edu); Guofeng Wang (guw8@pitt.edu); Ying Li (yingli@tamu.edu)

Abstract: Developing earth-abundant efficient catalysts for CO_2 reduction reaction (CO_2RR) is of paramount importance for electrochemical conversion of CO_2 into value-added products. Despite numerous studies on iron and nitrogen codoped carbon (Fe-N-C) catalysts, grand challenges exist due to limited performance and understanding of catalytic mechanisms. This study reports a general strategy to boost electrocatalytic CO_2RR activity of Fe-N-C with the incorporation of S atoms to engineer carbon support structure and electronic properties of active Fe−N sites simultaneously via a copolymer-assisted synthetic approach. The employment of N,S comonomers significantly increases the numbers of micropores and surface area, enabling dense atomic Fe−N and enhanced utilization efficiency. The first-principles calculations reveal that S modulation upraises the Fermi energy of Fe 3d and increases charge density on Fe atoms of $Fe-N_4$, thereby enhancing intrinsic catalytic reactivity and selectivity for CO_2 reduction by strengthening the binding interaction between the Fe site and key COOH* intermediate. These integrated structural and electronic merits endow Fe-NS-C with outstanding activity (e.g., CO Faradaic efficiency of 98% at an overpotential of 490 mV) and stability (without deactivation in 30 h), ranking it one of the most active Fe-N-C reported to date. The finding offers an innovative design strategy to enable the design of advanced catalysts for CO_2 conversion.

Keywords: CO_2 reduction, electrocatalysis, Fe-N-C, sulfur engineering, density functional theory

1. Introduction

Electrochemical CO_2 conversion under ambient conditions presents a promising way to synthesize value-added feedstock and reduce atmospheric CO_2 concentration simultaneously, where CO_2 reduction reaction (CO_2RR) take place at the cathode and water oxidization producing oxygen occurs at the anode.[1, 2] Extensive progress has been made for the anodic water oxidization,[3-6] but the cathodic CO_2RR has been investigated more rarely. In fact, CO_2RR is the cornerstone of CO_2 electro-conversion technology because it not only suffers sluggish kinetics and diversity of reaction routes,

but also competition with hydrogen evolution reaction (HER) in the aqueous phase.[7-9] In a variety of CO_2RR pathways and products, the reduction of CO_2 to CO has been predicted to be more practically economic due to less energy input required and high selectivity. Currently, noble metals Au and Ag are the state-of-the-art catalysts to drive CO_2 reduction to CO,[9] whereas the shortcomings of prohibitive cost and supply scarcity preclude their massive implementation. Thus, it is highly needed to develop earth-abundant CO_2-to-CO electrocatalysts with exceptional activity, selectivity, and durability.

Among non-precious metal catalysts explored, heat-treated transition metal and nitrogen codoped carbons (M-N-C) have emerged as promising alternatives to noble materials for CO_2RR where metal component is usually Fe or Ni.[10-13] In M-N-C, N-coordinated M complexes ($M-N_X$, especially $M-N_4$) are likely catalytic sites thanks to their optimal binding strength with reaction intermediates,[10-13] while carbon serves as the support to anchor $M-N_X$ and transfer electrons. Recently, many Ni-N-C materials have been developed for CO generation exhibiting high current density larger than 10 mA cm^{-2} and Faradaic efficiency more than 95%.[14, 15] However, Fe-N-C, another type of CO_2RR catalysts with inexpensive and earth-abundant properties, still exhibits a performance gap as compared to that required for economic viability. There also lacks of fundamental understanding of catalytic mechanisms and general design principles to develop Fe-N-C having high-density accessible $Fe-N_X$ sites with enhanced intrinsic catalytic reactivity.

To increase the number of Fe−N sites, an effective approach is to disperse Fe in the single atomic form since atomically dispersed Fe could achieve the maximum Fe atom use efficiency.[16] However, the Fe atoms have the tendency to aggregate into clusters or particles due to the migration and coalescence of atomic Fe species during the high-temperature annealing process.[17, 18] Previous studies demonstrated that single metal atoms are preferentially located at the micropores of carbon supports that serve as hosts to anchor metal atoms and provide stabilizing effects to hinder their sintering.[19-22] It is thus conceivable that constructing micropores could effectively improve dispersity of atomic Fe, allowing a higher probability for Fe atoms to coordinate with N atoms at the

edges of micropores to form adequate catalytically active Fe−N_X. In addition, an ideal Fe-N-C is expected to have a high surface area to maximize the exposure of Fe sites and make them fully accessible to reactants at the gas/solid/liquid tri-phase interface. [17, 18, 23]

Regarding the inherent catalytic nature of Fe−N_X, it is governed by the local electronic properties of Fe atoms.[24-27] Recent studies have demonstrated that the local electronic structure of Fe centers can be engineered by modifying their surrounding electronic environment by incorporating suitable heteroatoms in the carbon support.[24, 28, 29] Indeed, the modulated Fe sites have been found to be able to promote electrochemical thermodynamics by lowering the activation energy barriers of the rate-limiting reaction pathway in oxygen electrocatalysis, despite the underlying catalytic mechanisms and engineering roles remain elusive.[24, 27-29] However, to the best of our knowledge, modulating electronic structure of Fe-N-C to regulate their electrocatalytic behaviors for CO_2 reduction has not been explored yet. Therefore, tailoring the density and catalytic reactivity of Fe−N_X simultaneously may lead to a breakthrough in high-efficiency CO_2 reduction by Fe-N-C catalysts.

Inspired by the aforementioned discussions, we here rationally developed a class of high-performance catalyst comprising atomically dispersed Fe anchored on N and S dual-doped microporous carbon layers (Fe-NS-C) with high surface area to drive CO_2 reduction. Our catalyst design is based on the following rationales. The dominant micropores could provide numerous locations to host dense atomic Fe atoms for facilitating the evolution of Fe−N_X as catalytic sites, and the large surface area could improve the accessibility of Fe−N_X to reactants. Further, secondary S atoms are incorporated to modulate the electronic properties of Fe−N_X through electron donation interactions, pointing to promote their intrinsic electrocatalytic reactivity and selectivity. With these considerations, we developed a polymerization-assisted strategy to experimentally fabricate model catalysts with a tunable microporosity and surface area, as well as controllable N,S sole or dual doping, which we then applied to investigate their catalytic CO_2RR behaviors. Theoretical density functional theory (DFT) computations were also performed to explore the engineering roles of doped S atoms on electronic properties of Fe−N_4 moieties and their catalytic mechanisms and reactivity

toward CO_2RR and HER. Consequently, these unique structure and compositions achieve integrated increases in numbers, catalytic capability, and utilization efficiency of $Fe{-}N_X$ simultaneously on Fe-NS-C, resulting in the top-level CO_2RR performance in Fe-N-C community.

2. Results and Discussion

The preparation of model catalysts was carried out by a polymerization-assisted approach (**Fig. 1**), which allows for tuning catalyst structure and compositions by adjusting the monomers (Table S1). In a typical synthesis of Fe-NS-C, the polymerization of ethylenedioxythiophene (EDTO) and acetonitrile in the presence of $FeCl_3$ yielded polymer-Fe composites (Fig. S1), which were converted into carbon layers with doping of Fe,N,S via pyrolyzing under argon atmosphere. Numerous FeS/Fe particles were also generated at this stage, with the catalyst being named as FeS@NC. Followed by acid etching to remove accessible FeS/Fe and second heating treatment, the finial Fe-NS-C with small amounts of active Fe atoms inserted in N,S-codoped carbon frameworks was obtained. We also optimized the electrocatalytic performance by adjusting the annealing temperature, and 900 ºC was the optimal heating temperature for the best CO_2RR activity (Fig. S2). In addition, thiophene was used to fabricate Fe-NS-C, which exhibited slightly lower CO_2RR activity as compared to the one prepared from EDTO (Fig. S3). Therefore, the EDTO-derived one heated at 900 ºC was employed as the representative Fe-NS-C to be compared with their counterparts described as follows. To explore respective roles of S and N, S-free Fe,N-doped carbon (Fe-N-C) and N-free Fe,S-doped carbon (Fe-S-C) were prepared using the same procedure except replacing EDTO with pyrrole and replacing acetonitrile with acetone, respectively.

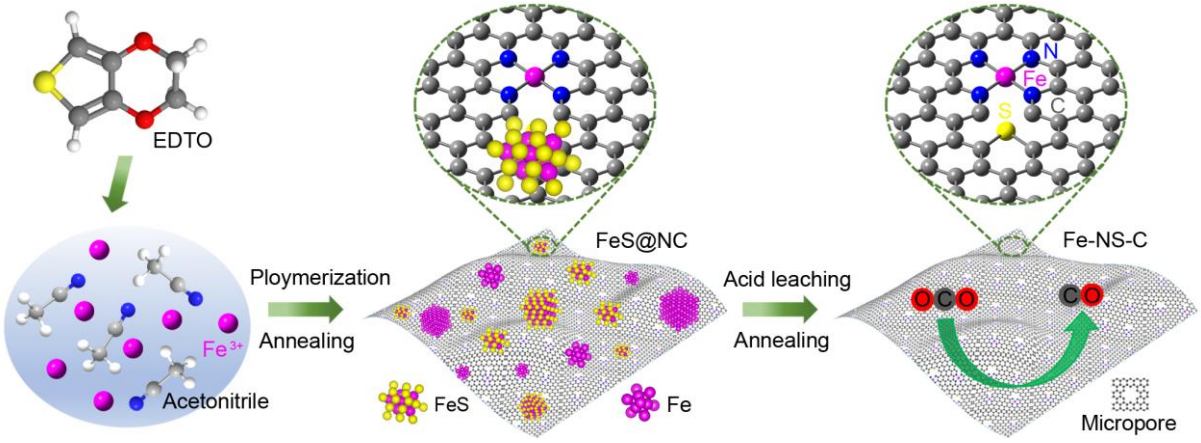

Fig. 1. Schematic illustration of the fabrication process for Fe-NS-C, showing the presence of abundant micropores and S-modulated Fe−N active sites.

Transmission electron microscopy (TEM) images (Fig. S4) show that FeS@NC possessed a wrinkled flake-like morphological feature with the presence of nanoparticles, which were identified as FeS, Fe, and Fe_3C by X-ray diffraction (XRD) (Fig. S5a). In contrast, Fe-NS-C retained the layer-structured morphology without large amounts of observable particulates (**Fig. 2a**). XRD patterns also show that peaks of Fe-related species disappeared in Fe-NS-C (Fig. S5b). These are evidence of the successful elimination of the majority of FeS/Fe with the post-treatment by acid. The high-resolution TEM image (**Fig. 2b**) displays distorted short-range graphitic stripes with wrinkles, interlaces, and fractures, suggesting the defective carbon structure; this might be caused by the local stress created by lattice defects, N,S dopants and carbon vacancies. Furthermore, the energy-dispersive X-ray mapping images (**Fig. 2c**) confirm the existence of C, O, N, S, and Fe species, which are homogeneously distributed in the carbon nanosheets. We noted that a very small amount of Fe particles also existed in Fe-NS-C (Fig. S6), which are typically encapsulated with multi-layer graphitic shells that protect them from being fully etched by acid.[18] Because these Fe-based particles fully sealed by thick carbon shells are inaccessible to aqueous and gaseous reactants, they are not expected to be able to participate in the electrochemical reactions and contribute to the catalytic activity of the catalysts.[18] Similar to Fe-NS-C, Fe-N-C possessed crumpled layer architecture with carbon-encased particles (Fig. S7), suggesting that they underwent the similar polymerization and carbonization processes.

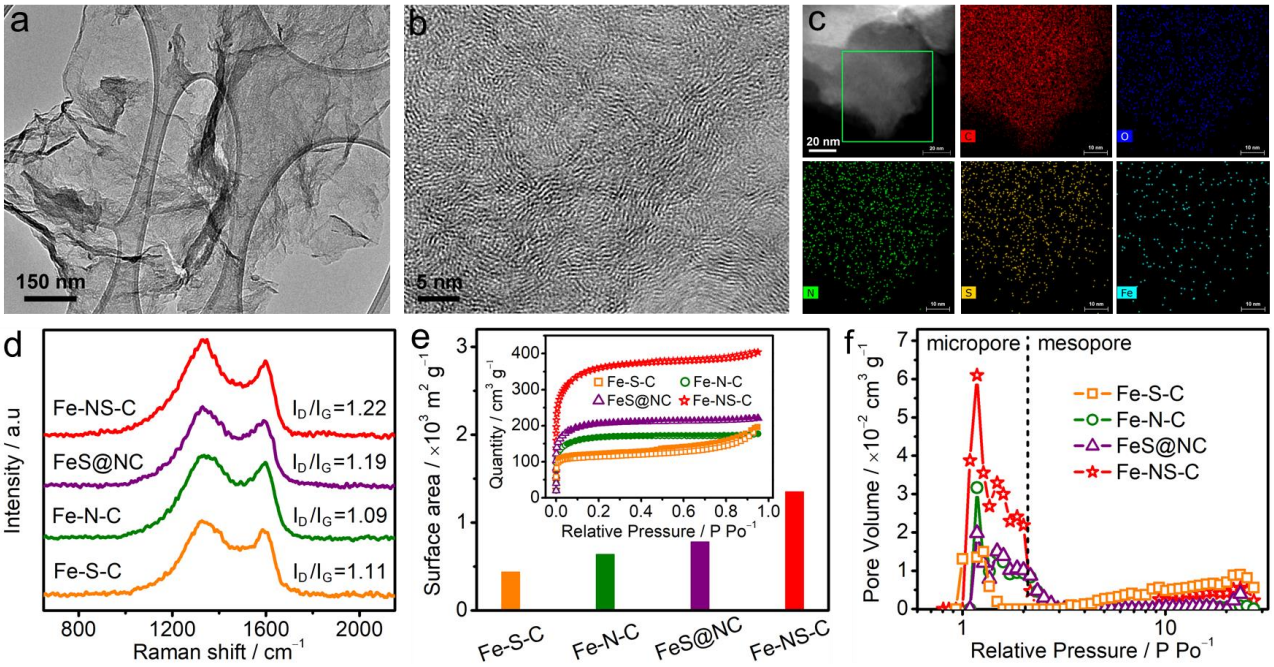

Fig. 2. (a) TEM and (b) high-resolution TEM, and (c) EDS elemental mapping images of Fe-NS-C. (d) Raman spectra, (e) BET surface area, and (f) pore size distributions for Fe-S-C, Fe-N-C, FeS@NC, and Fe-NS-C. Inserts of Fig. 1e are N_2 adsorption-desorption isotherms.

Raman spectroscopy exhibits two peaks at 1352 and 1580 cm^{-1} (**Fig. 2d**), which correspond to the disordered sp^3 carbon (D-band) and graphitic sp^2 carbon (G-band), respectively.[30, 31] The intensity ratios of D and G band (I_D/I_G) were calculated to be 1.11, 1.08, 1.19, and 1.22 for Fe-S-C, Fe-N-C, FeS@NC, and Fe-NS-C, respectively. It can be thus inferred that Fe-S-C possessed a slightly larger degree of defects than Fe-N-C, which is likely as a result of the larger radius of S relative to that of C and N; incorporating S is more likely to create defects due to the steric resistance that may break the integrity of hexagonal carbon honeycomb frameworks.[32] Furthermore, more defects were generated in N,S dual-doped ones compared to single N- or S-doped ones because of the codoping effects.

Nitrogen adsorption/desorption isotherm curves display steep increases in adsorbed quantity at relatively low N_2 partial pressures less than 0.1 and no significant increases at high pressures (**Fig. 2e**), reflecting the presence of dense micropores. Fe-NS-C possessed a Brunauer–Emmett–Teller (BET) surface area of 1353 $m^2\ g^{-1}$, much larger than that of FeS@NC (782 $m^2\ g^{-1}$). This suggests that the dissolution of FeS/Fe plays a key role in increasing the surface area because of the creation

of additional hierarchical pores. In addition, the surface area of Fe-NS-C is also significantly larger than that of Fe-N-C (639 $m^2 g^{-1}$) and Fe-S-C (440 $m^2 g^{-1}$). **Fig. 2f** shows the pore size distributions. Obviously, all samples had large percentages of micropores and small portions of mesopores, in which Fe-NS-C showed far more microporosity than others. These observations manifest that employing N,S comonomers as synthetic feedstock is crucial for achieving increased surface area and micropores. Previous report demonstrates that the decomposition of heteroatoms-containing groups in the carbonization process is responsible for the evolution of micropores in the carbon frameworks.[18] Accordingly, using both N and S monomers could provide sufficient heteroatoms species as sacrificial templates to direct the generation of abundant micropores after being thermally disintegrated.

X-ray photoelectron spectroscopy (XPS) survey spectra reveal the realization of the controllable synthesis of model catalysts with S and N being separately or collectively doped in the carbon (Fig. S8a). The N contents were calculated to be 0, 3.32, 4.18, and 3.80 at.% in Fe-S-C, Fe-N-C, FeS@NC, and Fe-NS-C, respectively, and the corresponding S contents are 2.03, 0, 2.16, and 1.76 at.% (Table S1), respectively. The high-resolution S 2p spectra (**Fig. 3a**) show the formation of C−S−C species (164.8 eV for $S2p_{3/2}$ and 165.8 eV for $S2p_{1/2}$) and oxidized S groups (C−SOx−C at 169.2 eV).[23, 33] In addition, N 1s spectra were deconvoluted into four peaks at 398.6, 400.5, 401.3 and 403.0 eV (**Fig. 3b**), which can be assigned to pyridinic (Pyri-N), pyrrolic (Pyrr-N), graphitic (Grap-N), and oxidized N (Oxid-N), respectively.[34, 35] The similar percentages of different N,S moieties in these catalysts (Table S2) imply that incorporating S atoms does not significantly affect the bonding configurations of N dopants. The actual Fe amounts, determined by inductively coupled plasma mass spectrometry (ICP-MC), are 0.55, 2.60, 20.2, and 1.82 wt.% in Fe-S-C, Fe-N-C, FeS@NC, and Fe-NS-C, respectively. From Fe 2p XPS spectra, we found that Fe-NS-C showed a Fe peak position at larger binding energy as compared to FeS@NC (Fig. S8b), manifesting that the oxidization state of Fe shifts to a higher value after removing FeS/Fe particles.

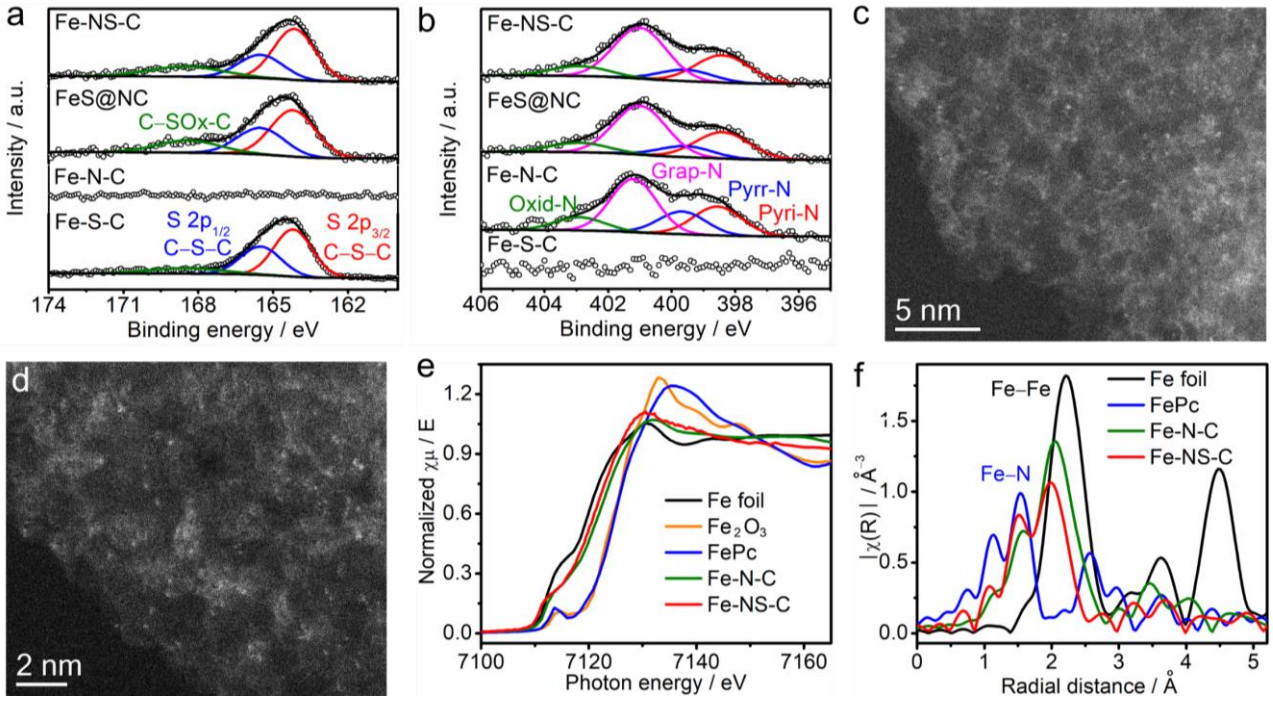

Fig. 3. (a) S 2p and (b) N 1s XPS spectra for Fe-S-C, Fe-N-C, FeS@NC, and Fe-NS-C. (c,d) HAADF-STEM images of Fe-NS-C. (e) XANES and (f) Fourier-transform EXAFS spectra of Fe-N-C, Fe-NS-C, and standard samples.

The atomic-level Fe distribution was visualized by high-angle angular dark-field scanning transmission electron microscopy (HAADF-STEM). As shown in **Fig. 3c,d**, the bright spots corresponding to heavy Fe atoms can be directly observed, which are densely dispersed in the carbon matrix. We further carried out X-ray absorption (XAS) measurements to unravel the chemical bonding environment of Fe species, where Fe foil, Fe_2O_3, iron phthalocyanine (FePc) were also characterized as standard references. **Fig. 3e** shows the typical X-ray absorption near-edge structure (XANES) spectrum of the Fe K-edge. The absorption of Fe-N-C and Fe-NS-C are located between Fe foil and Fe_2O_3, indicating that the average oxidation state of Fe atoms is in between Fe^0 and Fe^{3+}.[35, 36] In addition, Fe-N-C showed weak pre-edge peaks at 7114 eV similar to that of FePc, which is regarded as a fingerprint of the Fe−N_4 square-planar structure. [37, 38] However, Fe-NS-C exhibited a typical shoulder at 7114 eV, which can be attributed to the presence of Fe_3C.[27] The possible coordination environment around Fe atoms was further analyzed using the k_2-weighted Fourier transforms of extended X-ray absorption fine structure (EXAFS) at the Fe K-edge. As depicted in **Fig. 3f**, Fe-NS-C and Fe-N-C exhibited two peaks at around 1.54 and 2.00 Å,

corresponding to the Fe−N contribution and Fe−Fe bond, respectively. This directly indicates the formation of Fe−N complexes by bonding between isolated Fe and N atoms. Note that the peak at 2.00 Å is slightly different with that of metallic Fe foil but close to that of Fe_3C,[17] further confirming the presence of Fe_3C. It is known that the magnitude of EXAFS depends on the number and type of the scattering atoms. According to the literature, the types of M-based species in the M-N-C catalyst system (such as atomic M−N, metallic metal, and metal compounds) are strongly dependent on the pyrolysis temperature,[39, 40] and adding other heteroatoms (such as S) will not affect the type of M−N coordination.[41] Because Fe-N-C and Fe-NS-C in this work were synthesized at the same temperature of 900 ^{o}C, it is thus more likely that Fe-NS-C and Fe-N-C may have the same structure of Fe-based species. It can be seen in **Fig. 3f** that Fe-NS-C showed a reduction in amplitude in the peak at 2.00 Å when compared to Fe-N-C, suggesting a possible decrease in the number of Fe−Fe coordination number. Additionally, it is notable that Fe-NS-C possessed a relatively higher peak intensity of Fe−N and a lower intensity of Fe−Fe as compared to Fe-N-C. Considering that both Fe-N-C and Fe-NS-C may possess the same type of Fe−N, it can be thus inferred that more Fe−N species may be generated in Fe-NS-C than that in Fe-N-C.[17] Beside EXAFS results, the pore size distribution analyses demonstrate that Fe-NS-C had a larger amount of micropores than Fe-N-C (**Fig. 2f**). Previous reports manifest that the micropore is beneficial to inhibit the aggregation of Fe atoms by confining them in the micropores with enhanced stabilizing effects,[19-21] it is thus possible that Fe-NS-C could provide large numbers of atomically dispersed Fe to bond with N atoms as compared to Fe-N-C with less amount of micropore. Therefore, the generation of Fe−N in Fe-NS-C might be drastically promoted, leading to the denser Fe−N population in Fe-NS-C than in Fe-N-C. However, due to the complex compositions and carbon nanostructure and difficulty in accurately accounting the number of isolated Fe atoms in the catalysts, there still lacks more solid evidence to confirm the higher density of Fe−N in Fe-NS-C than Fe-N-C, which needs to be investigated in the future research.

The electrocatalytic CO_2RR activity was evaluated in an H-type cell with a standard three-electrode configuration. Fig. S9a depicts linear sweep voltammetry (LSV) curves recorded in both Ar- and CO_2-saturated 0.1 M $KHCO_3$ with a catalyst mass loading of 0.2 mg cm^{-2}. The LSV current in the Ar-saturated solution is from the reduction of proton to H_2. When the Ar supply was replaced by CO_2, the reaction current increases and the onset potential shifts positively, implying the occurrence of CO_2 reduction. **Fig. 4a** shows LSV comparisons of four model catalysts in the CO_2-saturated electrolyte. Among them, Fe-S-C exhibited extremely low currents, implying its poor activity. In contrast, Fe-NS-C displayed significantly larger currents than Fe-N-C and FeS@NC, suggesting that it is the doped S atoms that contribute to the substantial enhancement in the catalytic rates of Fe-N-C.

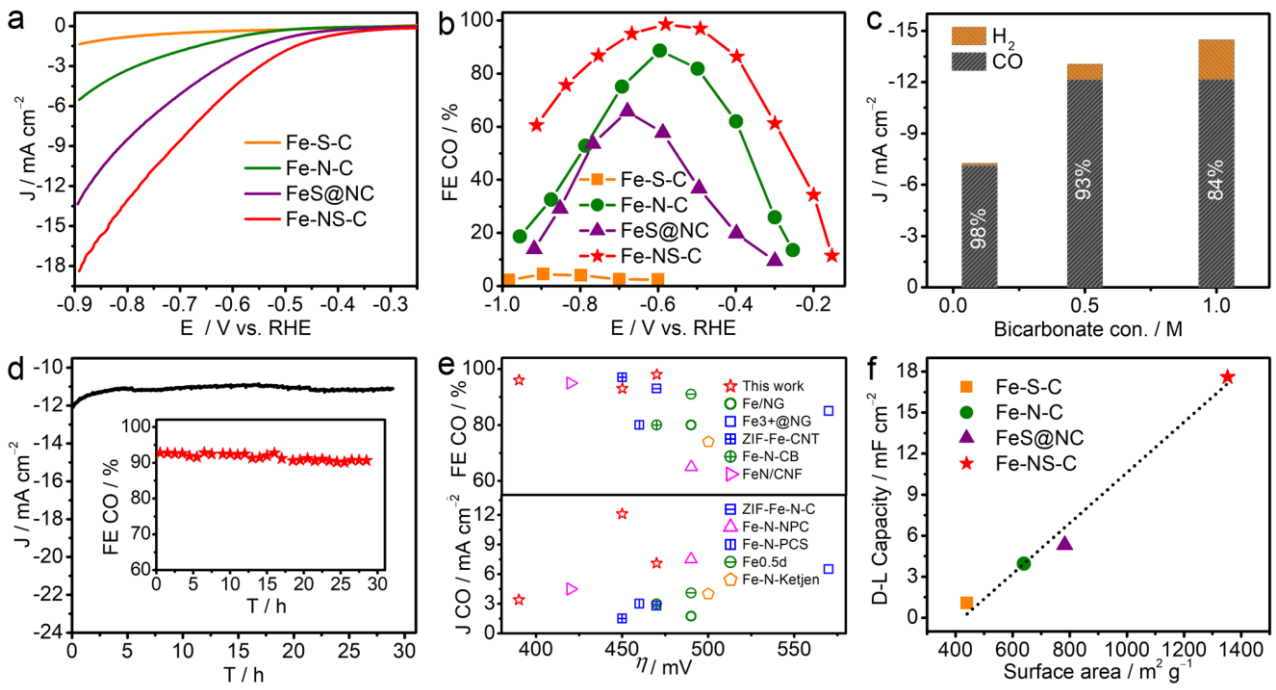

Fig. 4. Electrocatalytic CO_2RR performance. (a) CO_2RR polarization curves and (b) CO FEs in 0.1 M $KHCO_3$ solution on Fe-S-C, Fe-N-C, FeS@NC, and Fe-NS-C with a catalyst mass loading of 0.2 mg cm^{-2}. (c) Total current density and maximum CO FEs of Fe-NS-C in 0.1, 0.5, and 1.0 M $KHCO_3$ solution with catalyst mass loading of 1 mg cm^{-2}. (d) Electrocatalytic CO_2RR stability of Fe-NS-C in 0.5 M $KHCO_3$ at −0.58 V. (e) CO_2 reduction activity comparisons between Fe-NS-C and reported Fe-N-C catalysts (Table S3). (f) Correlation of double layer capacity and BET surface area of the model catalysts.

The constant potential electrolysis was further conducted to determine catalytic activity and product selectivity. CO and H_2 are the main gaseous products detected by an on-line gas

chromatograph with total Faradaic efficiency (FE) near 99%, and no liquid-phase products were detected by ^{1}H nuclear magnetic resonance (NMR). The total current density presents that Fe-NS-C delivered the highest currents in the all potential region (Fig. S9b), followed by FeS@NC, Fe-N-C, and Fe-S-C. Potential-dependent CO FEs are depicted in **Fig. 4b**, in which Fe-S-C exhibited extremely low CO FEs below 5%, uncovering the catalytically inert nature of Fe,S,O,C-based species towards CO_2RR. As for Fe-N-C, CO_2 reduction started at −0.25 V with a CO FE of 15%, showing an onset overpotential of 140 mV given that the equilibrium potential of CO_2/CO couple is −0.11 V.[42] The CO FEs rapidly increased to a maximum value of 89% at an overpotential of 480 mV and then decreased as the applied potentials sweep more negatively. Because we could not be able to prepare Fe-free N-C as a suitable counterpart using the same synthesis approach to Fe-N-C due to the necessity of $FeCl_3$ as oxidant in the ploymerization of pyrrole in acetonitrile solution, we could not study the role of Fe in Fe-N-C for CO_2 reduction here. In our previsou work, we have systematically investigated the role of Fe in Fe-N-C catalyst toward CO_2RR by comparing the catalytic CO_2RR behaviors on both Fe-N-C and N-C prepared using the same method,[12] and we found that adding Fe in N-C significantly lowered the onset overpotential and increased both CO FE and current density. Similarly, other previous works have also manifested the enhanced catalytic properties of Fe-N-C for CO_2RR as compard to C-N.[10, 43] All these results demonstrate that Fe−Nx species is intrinsically more active and selective than C−Nx and thus might be the decisive catalytic site for CO_2RR in Fe-N-C.

In the case of Fe-NS-C, it generated CO at an overpotential of 40 mV, which is 100 mV smaller than that of Fe-N-C. The highest CO FE reached 98% at an overpotential of 470 mV, 9% larger than that of Fe-N-C. On the other hand, FeS@NC showed an onset overpotential of 190 mV and a maximum CO FE of 64% at an overpotential of 590 mV, which are worse relative to those of Fe-N-C and Fe-NS-C. This signifies that FeS/Fe particles are not active species toward CO_2 reduction. Tafel plots show that Fe-NS-C possessed a smaller Tafel slope of 101 mV dec^{-1} than Fe-N-C (114 mV dec^{-1}) and FeS@NC (116 mV dec^{-1}), manifesting a faster CO_2RR kinetics on Fe-NS-C surface

(Fig. S9d). [43] Furthermore, the Tafel slope, near 118 mV dec^{-1}, indicates that the first electron transfer, which generates surface adsorbed *COOH species, is the rate-determining step in the CO evolution process.[44] The elementary reaction steps are schematically depicted in Fig. S10. In the fist step, CO_2 is activated to *COOH intermediate via concerted proton-coupled electron transfer process ($CO_2 + H^+ + e^- + * \rightarrow$ *COOH). In the second step, *COOH combines with another electron and proton, forming *CO and H_2O (*COOH + $H^+ + e^- \rightarrow$ *CO + H_2O). Finally, the desorption of CO releases gaseous CO as the final product (*CO $\rightarrow$ CO). By combining the electrochemical results with compositions of the catalysts, it can be concluded that Fe−N_X is the main catalytic site in CO_2RR, and the doped S atoms might function as promoters that play key roles in decreasing overpotentials and accelerating the overall CO_2 reduction rates.

We further investigated the effects of catalyst mass loading and electrolyte concentrations on CO_2RR activity and selectivity. As can be seen in Fig. S11-S13, current density depends strongly on both the amounts of Fe-NS-C coated on the electrode and $KHCO_3$ concentrations, while the CO FE is only dependent on the electrolyte concentration. Note that, although total current density increases with increasing catalyst loading, it shows a non-proportional enhancement as a function of mass loading. This can be ascribed to the influences of poor mass transportation and decreased accessibility to the active sites due to the stacking of Fe-NS-C nanosheets in a thicker catalyst layer. In addition, we found that a more concentrated electrolyte gives rise to larger current densities (Fig. S13); however, it causes the decline in CO selectivity, which decreased from 98% in 0.1 M solution at −0.58 V to 93% in 0.5 M solution at −0.56 V and to 84% in 1 M solution at −0.53 V (**Fig. 4c**). These observations indicate that the HCO_3^- concentration greatly impacts the efficiency of electrochemical CO_2 reduction, in consistence with reported studies on Fe-N-C and Au electrodes wherein a higher concentration of HCO_3^- can boost the overall reaction rate but is at the expense of lower CO FEs.[13, 45] In CO_2 reduction condition, the HCO_3^- not only acts as a pH buffer and proton donor but it also affects the concentration of CO_2. An elevated local pH in a concentrated $KHCO_3$ solution may preserve a high interfacial CO_2 concentration near the electrode surface owing to the suppressed

equilibration between CO_2 and bicarbonate by slowing the CO_2 hydration kinetics,[45] therefore accelerating the CO production. As a result, we obtained a CO current density of 12.1 mA cm^{-2} in 0.5 M $KHCO_3$ with CO FEs of 93%. Finally, we tested the electrochemical stability of Fe-NS-C, which retained stable currents of 11 mA cm^{-2} and CO FE above 90% after a 30 h continuous operation in 0.5 M $KHCO_3$ (**Fig. 4d**). When compared with reported Fe-N-C (**Fig. 4e**, Table S3), it is conspicuous that our Fe-NS-C almost outperforms all of them at a similar condition, highlighting the great promise of the S modulation in boosting CO_2RR activity and selectivity for Fe-N-C catalysts. To demonstrate the possibility of using Fe-NS-C to replace noble metals, CO_2 reduction activity of comercial Ag and Au nanoparticels were tested in CO_2-saturated 0.5 M $KHCO_3$ solution with a catalyst mass loading of 0.5 mg cm^{-2}. As can be seen in Fig. S14, Fe-NS-C had larger CO FE and partial current than Ag NPs at potential positive than −0.7 V. When compared with Au, Fe-NS-C showed higher current and similar FE for CO generation at −0.3 ~ −0.6 V. These comparisons results indicate that Fe-NS-C is a promising alternative to precious metals for electrocatalytic CO_2-to-CO conversion.

In the electrocatalytic reaction over carbon catalysts, the overall catalytic performance is highly governed by both extrinsic physicochemical properties of carbon support and electronic properties of active sites, which determines the number of effective active sites and their intrinsic catalytic reactivity, respectively.[46, 47] By correlating CO_2RR activity with carbon architecture and compositions of model catalysts, the superior electrocatalytic performance of Fe-NS-C can be ascribed to the integrated benefits induced by highly microporous nanostructure of the carbon support with large surface area and S atoms engineering. Firstly, the large amounts of micropores in Fe-NS-C provide numerous caves to anchor isolated Fe atoms, benefiting the formation of abundant $Fe{-}N_X$ as the main active species for CO_2RR and OER, as evidenced by EXAFS. Secondly, a larger surface area could afford an improved interfacial contact between solid catalyst and liquid electrolyte. To demonstrate this, we estimated electrochemical active surface area (ECSA) by measuring double layer (D-L) capacitance, since ECSA is proportional to capacitance.[48, 49] As shown in Fig. S15,

Fe-NS-C exhibited a DL-capacity of 17.6 mF cm^{-2}, much larger than that of Fe-S-C (1.08 mF cm^{-2}), Fe-N-C (3.95 mF cm^{-2}), and FeS@NC (5.32 mF cm^{-2}). Upon plotting capacitance as a function of surface area (**Fig. 4f)**, it gives a positive linear correlation, validating that the larger surface area of Fe-NS-C is beneficial to enhance the exposure of active sites on the carbon layer surface and thus improve their utilization efficiency. Thirdly, the doped S atoms could modulate the electronic properties of $Fe{-}N_X$ sites because the S incorporation may lead to the redistribution of charge on Fe sites.[28] Consequently, the S engineering could tailor the intrinsic catalytic nature of $Fe{-}N_X$ and make great contributions to boosting the CO_2RR performance, as evidenced by the following theoretical calculations.

To gain insights into the electrocatalytic mechanisms, theoretical DFT calculations were performed using the computational hydrogen electrode method. In consistence with previous studies that one Fe atom is more likely to coordinate with four N atoms forming the energetically stable $Fe{-}N_4$ structure, [18, 50, 51] we constructed a $Fe{-}N_4$ moiety embedded in the carbon matrix representing the possible active site of Fe-N-C (**Fig. 5a**). Considering that S has a significantly larger atomic radius than C, it is more likely that incorporating S atoms into the carbon lattice is accompanied by the creation of carbon vacancies.[32, 52] We thus built two S-modified $Fe{-}N_4$ moieties with one S atom ($Fe{-}N_4$+1S) and two S atoms ($Fe{-}N_4$+2S) with the existence of the carbon vacancies to model the possible active sites structure of Fe-NS-C.

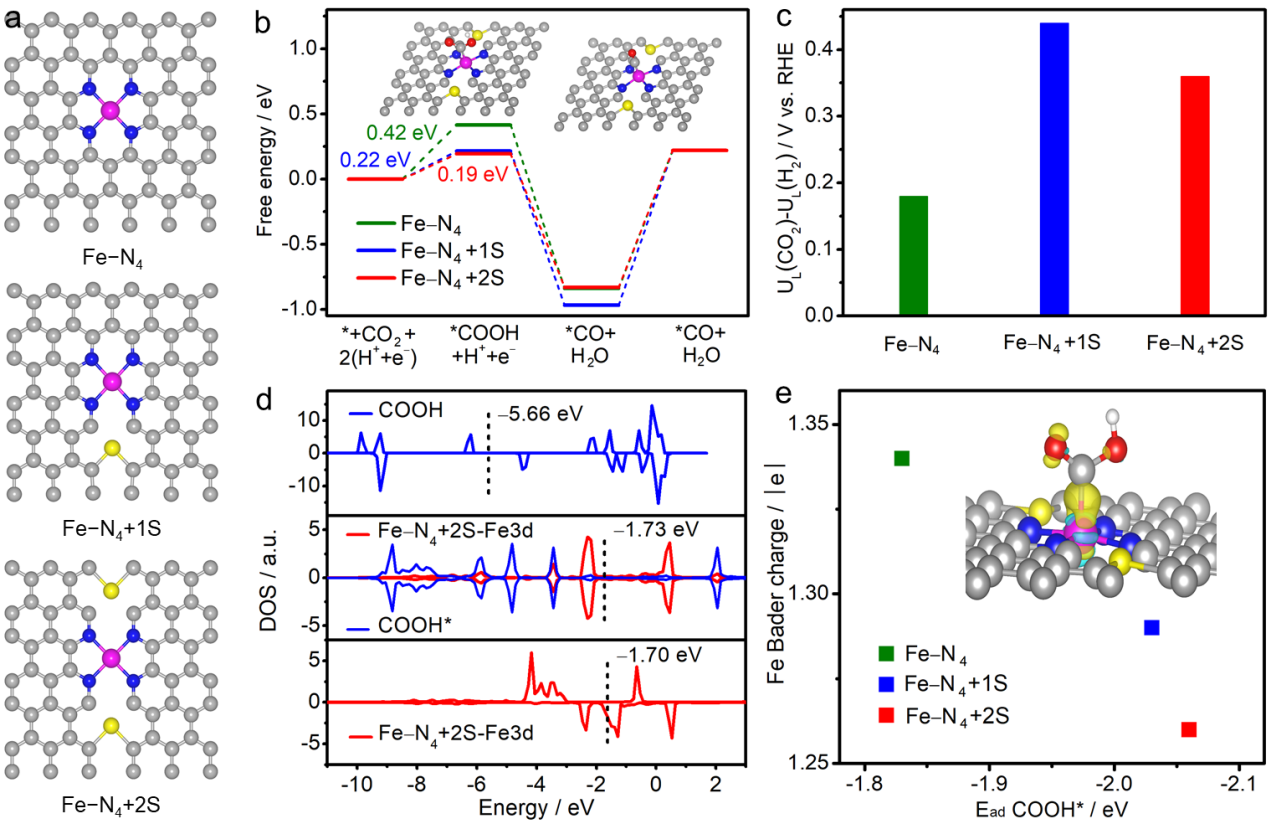

Fig. 5. (a) Atomic structure of proposed Fe−N_4 and S-modified Fe−N_4 moieties. (b) Free energy diagrams of CO_2RR at the electrode potential of U=0 V. Inserts of b are the optimized adsorption configurations of COOH* and CO* on Fe−N_4+2S. (c) Difference in limiting potentials between CO_2 reduction and H_2 evolution. (d) Density of states for Fe 3d of Fe−N_4+2S, COOH and Fe−N_4+2S-COOH*. (e) Calculated adsorption energy of COOH* and Fe Bader charge. Insert is the charge density difference for COOH* adsorbed on Fe−N_4+2S, which is computed as ρ(Fe−N_4+2S-COOH*)-ρ(Fe−N_4+2S)-ρ(COOH). Cyan and yellow represent charge accumulation and depletion in the region; the isosurface value is 0.01 e $Å^{-3}$. In the figure, the gray, blue, purple, yellow, red, and white balls represent C, N, Fe, S, O, and H atoms, respectively.

In calculating free-energy barriers for CO_2 reduction, we considered the reaction mechanism of CO_2RR to CO through forming the well-accepted COOH* and CO* as adsorbed intermediates (Fig. S16,S17).[11, 36] **Fig. 5b** depicts the Gibbs free energy diagram for CO_2 reduction, which reveals that the first proton-coupled electron transfer to form COOH* is the potential-limiting step on all active sites. Compared to Fe−N_4 that exhibited a free-energy barrier of 0.42 eV, it is notable that incorporating an S atom significantly decreases the free-energy barrier, showing a low barrier of 0.22 eV on Fe−N_4+1S. The free energy barrier can be further reduced to 0.19 eV on Fe−N_4+2S. These results clearly demonstrate that the S modification reduces the barrier for CO_2 activation on Fe−N_4,

consistent with the experimental observation that Fe-NS-C showed lower onset overpotentials than Fe-N-C for CO production.

Because proton reduction to H_2 is the major competitive reaction that can decrease the CO_2RR selectivity, we further studied the effects of S incorporation on catalytic capability of $Fe{-}N_4$ for H_2 evolution. Fig. S18a depicts the LSV curves recorded in the Ar-saturated solution. It was observed that Fe-NS-C showed larger LSV current than Fe-N-C, suggesting that the hydrogen production rate on Fe-NS-C is larger than that of Fe-N-C. The Gibbs free energies for hydrogen evolution were also calculated. As can be seen in Fig. S18b that $Fe{-}N_4$+1S showed a free energy barrier of 0.66 eV, which is 0.06 eV larger than that of $Fe{-}N_4$ (0.60 eV). As for $Fe{-}N_4$+2S, it exhibited a free energy barrier of 0.56 eV, 0.04 eV smaller than that of $Fe{-}N_4$. These results imply that adding S in Fe-N-C does not significantly affect the catalytic capability of $Fe{-}N_4$ sites for hydrogen evolution. Therefore, the observed enhancement in LSV current under Ar-saturated solution can be attributed to the higher surface area and denser $Fe{-}N_4$ sites on Fe-NS-C as compared to Fe-N-C. In the CO_2 reduction process, there exists the competition between CO_2 reduction and H_2 evolution. Considering that incorporating S plays a neglectable role in affecting on catalytic properties of $Fe{-}N_4$ for H_2 evolution but drasctically promoting CO_2 reduction, FEs for the reduction of CO_2 to CO could thus be improved on Fe-NS-C in comparison to Fe-N-C; accordingly, observed FEs for H_2 production decreased. Previous studies have proposed that the difference between thermodynamic limiting potentials for CO_2RR and HER, denoted as $U_L(CO_2) - U_L(H_2)$ ($U_L = -G_0/e$), can act as a descriptor to gauge the selectivity for CO_2RR-generated products;[43] a larger positive $U_L(CO_2) - U_L(H_2)$ value corresponds to a better selectivity toward CO_2 reduction. As shown in **Fig. 5c**, two S-modified $Fe{-}N_4$ were predicted to have larger positive $U_L(CO_2) - U_L(H_2)$ values than pristine $Fe{-}N_4$, suggesting that doping S atoms enhances the catalytic selectivity of $Fe{-}N_4$ for CO production. These results supports our experimental findings that Fe-NS-C exhibited higher CO FEs than Fe-N-C.

To unveil the underlying roles of S engineering in impacting the catalytic origin of Fe sites, the electronic density of state was analyzed. Our calculations demonstrate that the orbital of Fe 3d of

proposed moieties and COOH adsorbate participate in orbital coupling during the adsorption of COOH on Fe sites, as revealed by their orbital overlap (**Fig. 5d**, Fig. S19). In addition, the Fermi energy of Fe 3d is located more positively than that of COOH, and the Fermi energy of Fe3d-COOH* is located in between that of Fe 3d and COOH* on all active sites. This observation suggests that the electrons are transferred from Fe centers to COOH* when the bond between Fe and COOH is formed. The electron transfer direction can be further verified by the calculated charge difference, in which the charge accumulation on COOH* occurs (insert of **Fig. 5e**). Furthermore, it was observed that the Fermi energy of Fe 3d shifted positively from −1.87 eV on Fe−N_4 to −1.71 eV on Fe−N_4+1S and −1.70 eV on Fe−N_4+2S (**Fig. 5d**, Fig. S19). The up-raised Fermi energy of Fe 3d can result in a faster electron transfer in the COOH adsorption thanks to the enhanced driving force caused by larger energy difference, thus promoting the adsorption of COOH* on S-modified Fe sites.

We also calculated the charge density of Fe centers for the proposed active sites. As can be noticed in **Fig. 5e**, the addition of S atoms leads to the decrease in Bader charge of Fe atoms from −1.34 eV on Fe−N_4 to −1.29 eV on Fe−N_4+1S and −1.26 eV on Fe−N_4+2S. The more negative charge suggests the increase in the density of valance electrons on Fe atoms upon the decoration of Fe−N_4 by S, which might be the result of the electron donation from the surrounding S atoms.[53, 54] The enhanced charge density can also make a contribution in speeding up the electron transfer and increasing the binding strength between Fe and COOH*.[55] The improved COOH* adsorption can, therefore, accelerate the CO_2RR kinetics on Fe-NS-C. Coupling computational and experimental results, we attributed the improved CO_2 reduction performance of Fe-NS-C to the synergistic merits induced by increased available numbers and intrinsic catalytic nature of S-engineered Fe−N_X sites.

3. Conclusion

In summary, we developed a powerful and versatile strategy of sulfur activation to promote CO_2 reduction electrocatalysis on Fe-N-C. Our findings show that the incorporation of S in the Fe-N-C synthesis results in numerous micropores and high surface area (1353 m^2 g^{-1}), which provide sites to

anchor dense atomically dispersed Fe−N_X and enables enhanced electrochemical active surface area, respectively. DFT calculations reveal that the S engineering upraises Fermi energy of Fe 3d and enriches the charge density of Fe center in Fe−N_4, thus lowering the energy barriers in the CO_2RR process by enhancing binding interaction between Fe sites and COOH* intermediate. These integrated structural and electronic benefits greatly boost electrocatalytic CO_2 reduction on Fe-NS-C, reaching the top-level performance among Fe-N-C community in terms of an CO Faradaic efficiency of 98% with a partial current of 7.1 mA cm^{-2} at an overpotential of 470 mV. Therefore, Fe-NS-C holds great promise of being implemented as a non-precious yet efficient catalyst to drive practical CO_2 electroconversion. More importantly, the catalysts design concepts of synergistically tailoring of the geometric architecture of support and electronic properties of single-atom metals will open up new opportunities for the rational design of high-performance catalysts for a spectrum of energy-related electrocatalytic processes.

4. Experimental Section

Catalysts Synthesis. In a typical synthesis of Fe-NS-C, a solution of $FeCl_3$ (3g) in acetonitrile (15 mL) was added dropwise into an ethylenedioxythiophene (EDOT, 0.3 g) (or thiophene) solution in acetonitrile (35 mL). The mixture was continuously stirred for 24 h at room temperature to ensure complete polymerization of the EDOT and acetonitrile and then heated at 80 ºC to remove un-polymerized precursors. The dried polymer-Fe composites were annealed at 900 ºC for 3 h to produce FeS@NC. After acid leaching with 2 M HCl for 10 h and 2 M HNO_3 for 10 h and heating treatment at 900 ºC for 1h, the obtained catalyst was denoted as Fe-NS-C. For comparison purpose, the N-free Fe,S-doped carbon (Fe-S-C) was prepared using the same method to Fe-NS-C but replacing acetonitrile with acetone, and S-free Fe,N-doped carbon (Fe-N-C) was fabricated by replacing EDOT with pyrrole.

Physical characterization. Morphology, structure, and composition of catalysts were characterized by transmission electron microscopy (TEM, FEI Tecnai G2 F20 ST), high-angle angular dark-field

scanning transmission electron microscopy (Hitachi 2700C), X-ray diffraction (XRD, BRIKER D8), Raman spectroscopy (Horiba Jobin-Yvon LabRam HR), and X-ray photoelectron spectroscopy (XPS, Omicron). Brunauer–Emmett–Teller (BET) surface area analysis was performed on a Micromeritics ASAP 2420 physisorption analyzer. The X-ray absorption spectroscopy (XAS) measurements were performed at the 20-BM station at The Advanced Photon Source at Argonne National Laboratory.

Electrochemical CO_2RR activity measurements. Electrocatalytic CO_2RR activity was evaluated in a two-compartment three-electrode electrochemical cell in CO_2-saturated $KHCO_3$ electrolyte. A Pt mesh and an Ag/AgCl (3M KCl) were used as the counter electrode and reference electrode, respectively. The measured potentials after iR compensation were rescaled to the reversible hydrogen electrode by E (RHE) = E (Ag/AgCl) + 0.210 V + 0.0591V×pH. The working electrode was prepared by drop casting catalyst ink onto a carbon paper. The ink was prepared by dispersing 3 mg catalysts in a mixture solution of 200 μL DI-water, 370 μL ethanol, and 30 μL 5% Nafion solution via sonication for 3 h. The catalysts mass loading was adjusted from 0.2, 0.5 to 1 mg cm^{-2} and the concentration of $KHCO_3$ was tuned from 0.1, 0.5 to 1 M for the sake of optimizing CO_2RR activity and selectivity. The working and reference electrodes were placed in the cathode chamber, while the counter electrode was placed in the anode chamber, which was separated by a piece of Nafion 115 ionic exchange membrane to avoid the re-oxidation of CO_2RR-generated products. The high-purity CO_2 was introduced in the cathode chamber for 1 h to saturate electrolyte before electrolysis with a flow rate of 34 ml min^{-1} and maintained this flow rate during measurements. The gas-phase products were analyzed via an online gas chromatograph (GC, Fuel Cell GC-2014ATF, Shimadzu) equipped with a thermal conductivity detector (TCD) and a methanizer assisted flame ionization detector (FID). No liquid-phase products were detected by ^{1}H Nuclear magnetic resonance (NMR).

Faradaic efficiency (FE) of gaseous products at each applied potential was calculated based on the equation:

$$\mathrm{FE} = \frac{z \cdot P \cdot F \cdot V \cdot v_i}{R \cdot T \cdot J}$$

Where z is the number of electrons transferred per mole of gas product (z is 2 for CO and H_2), F is Faraday constant (96500 C mol^{-1}), P is pressure (1.01×10^5 Pa), V is the gas volumetric flow rate (5.67×10^{-7} m^3 s^{-1}), v_i is the volume concentration of gas product determined by GC, T is the temperature (298.15 K), R is the gas constant (8.314 J mol^{-1} K^{-1}), and J is the steady-state current at each applied potential (A).

Density functional theory (DFT) calculations. Structure optimization and electronic energy calculations were performed using the first principles spin-polarized DFT method as implemented in the Vienna ab initio simulation package (VASP) code. Projector augmented wave (PAW) pseudopotential was employed to describe the core electrons. The cutoff energy was set as 400 eV to expand the wave functions. Electronic exchange and correction were described by generalized gradient approximation (GGA) of the revised Perdew, Burke and Ernzernhof (RPBE) functionals. Various Fe−N_4 and S-modified Fe−N_4 models were constructed as the active sites for CO_2RR. The Brillouin Zone was sampled by 3×3×1 Monkhorst-pack k-point meshes for the Fe-N_4,Fe-N_4+1S and Fe-N_4+2S active site models. For each structure, the atomic positions were optimized until the force fell below 0.01eV/ Å.

The computational hydrogen electrode (CHE) was used to calculate the free energy of each intermediate state from reactants to products.[56] The free energy of a chemical reaction is calculated by

$$\Delta G = \Delta E_{DFT} + \Delta E_{ZPE} + \Delta E_{solv} + \Delta H_{0\ to\ T} - T\Delta S$$

where ΔE_{DFT} is the energy change calculated by DFT method, ΔE_{ZPE} is the zero-point energy correction, ΔE_{solv} is the solvation energy correction, $\Delta H_{0\ to\ T}$ is the reaction enthalpy change from 0 to T K, and ΔS is reaction entropy change. The solvation effect correction was 0.25 eV stabilization of COOH*, 0.1 eV stabilization of CO*. ZPE corrections were calculated as ZPE =$\sum \frac{1}{2} h v_i$, where h is Planck's constant and v_i is the frequency of the corresponding vibrational mode of binding molecules. $\Delta H_{0\ to\ T}$ was calculated by the vibrational heat capacity integration $\int_0^t C_p dT$. The entropy terms for

gas phase were derived from partition functions and compared with the data from NIST Standard reference database.

Acknowledgments

Y. Li, G. Wang, and G. Wu acknowledges the support for a collaborative project from U.S. National Science Foundation (NSF CBET #1805132, #1804534, and #1804326). T. Li is thankful for the support from NIU startup. G. Wang gratefully acknowledges the computational resources provided by the University of Pittsburgh Center for Research Computing as well as the Extreme Science and Engineering Discovery Environment (XSEDE), which is supported by National Science Foundation grant number ACI-1053575. Use of the Advanced Photon Source at Argonne National Laboratory was supported by the US Department of Energy (DOE), Office of Science, and Office of Basic Energy Sciences.

Appendix A. Supporting Information

Supplementary data associated with this article can be found in the online version at

References

[1] M. Asadi, K. Kim, C. Liu, A.V. Addepalli, P. Abbasi, P. Yasaei, P. Phillips, A. Behranginia, J.M. Cerrato, R. Haasch, P. Zapol, B. Kumar, R.F. Klie, J. Abiade, L.A. Curtiss, A. Salehi-Khojin, Science 353 (2016) 467-470.
[2] J.M. Spurgeon, B. Kumar, Energy Environ. Sci. 11 (2018) 1536-1551.
[3] W. Gao, Z. Xia, F. Cao, J.C. Ho, Z. Jiang, Y. Qu, Adv Funct Mater 28 (2018) 1706056.
[4] Z. Cai, X. Bu, P. Wang, J.C. Ho, J. Yang, X. Wang, Journal of Materials Chemistry A 7 (2019) 5069-5089.
[5] A. Alarawi, V. Ramalingam, J.-H. He, Materials Today Energy 11 (2019) 1-23.
[6] A. Alarawi, V. Ramalingam, H.-C. Fu, P. Varadhan, R. Yang, J.-H. He, Opt Express 27 (2019) A352-A363.
[7] K.P. Kuhl, E.R. Cave, D.N. Abram, T.F. Jaramillo, Energy & Environmental Science 5 (2012) 7050-7059.
[8] J. Wu, S. Ma, J. Sun, J.I. Gold, C. Tiwary, B. Kim, L. Zhu, N. Chopra, I.N. Odeh, R. Vajtai, A.Z. Yu, R. Luo, J. Lou, G. Ding, P.J.A. Kenis, P.M. Ajayan, Nature Communications 7 (2016) 13869.
[9] Q. Lu, F. Jiao, Nano Energy 29 (2016) 439-456.
[10] C. Zhang, S. Yang, J. Wu, M. Liu, S. Yazdi, M. Ren, J. Sha, J. Zhong, K. Nie, A.S. Jalilov, Z. Li, H. Li, B.I. Yakobson, Q. Wu, E. Ringe, H. Xu, P.M. Ajayan, J.M. Tour, Advanced Energy Materials 8 (2018) 1703487.

[11] W. Ju, A. Bagger, G.-P. Hao, A.S. Varela, I. Sinev, V. Bon, B. Roldan Cuenya, S. Kaskel, J. Rossmeisl, P. Strasser, Nature Communications 8 (2017) 944.
[12] F. Pan, W. Deng, C. Justiniano, Y. Li, Appl. Catal. B: Environ. 226 (2018) 463-472.
[13] T.N. Huan, N. Ranjbar, G. Rousse, M. Sougrati, A. Zitolo, V. Mougel, F. Jaouen, M. Fontecave, ACS Catalysis 7 (2017) 1520-1525.
[14] T. Zheng, K. Jiang, N. Ta, Y. Hu, J. Zeng, J. Liu, H. Wang, Joule 3 (2019) 265-278.
[15] H.B. Yang, S.-F. Hung, S. Liu, K. Yuan, S. Miao, L. Zhang, X. Huang, H.-Y. Wang, W. Cai, R. Chen, J. Gao, X. Yang, W. Chen, Y. Huang, H.M. Chen, C.M. Li, T. Zhang, B. Liu, Nature Energy 3 (2018) 140-147.
[16] Y. Chen, S. Ji, C. Chen, Q. Peng, D. Wang, Y. Li, Joule 2 (2018) 1242-1264.
[17] B.-C. Hu, Z.-Y. Wu, S.-Q. Chu, H.-W. Zhu, H.-W. Liang, J. Zhang, S.-H. Yu, Energy & Environmental Science 11 (2018) 2208-2215
[18] H.T. Chung, D.A. Cullen, D. Higgins, B.T. Sneed, E.F. Holby, K.L. More, P. Zelenay, Science 357 (2017) 479-484.
[19] M. Lefèvre, E. Proietti, F. Jaouen, J.P. Dodelet, Science 324 (2009) 71-74.
[20] Y. Tang, Y. Li, V. Fung, D.-e. Jiang, W. Huang, S. Zhang, Y. Iwasawa, T. Sakata, L. Nguyen, X. Zhang, A.I. Frenkel, F. Tao, Nature Communications 9 (2018) 1231.
[21] L. Zhang, Y. Ren, W. Liu, A. Wang, T. Zhang, National Science Review 5 (2018) 653-672.
[22] F. Jaouen, M. Lefèvre, J.-P. Dodelet, M. Cai, The Journal of Physical Chemistry B 110 (2006) 5553-5558.
[23] L. Chen, J. Han, Y. Ito, T. Fujita, G. Huang, K. Hu, A. Hirata, K. Watanabe, M. Chen, Angewandte Chemie International Edition 57 (2018) 13302-13307.
[24] Y. Han, Y. Wang, R. Xu, W. Chen, L. Zheng, A. Han, Y. Zhu, J. Zhang, H. Zhang, J. Luo, C. Chen, Q. Peng, D. Wang, Y. Li, Energy & Environmental Science 11 (2018) 2348-2352.
[25] F. Razmjooei, K.P. Singh, D.-S. Yang, W. Cui, Y.H. Jang, J.-S. Yu, ACS Catalysis 7 (2017) 2381-2391.
[26] H.-C. Huang, Y.-C. Lin, S.-T. Chang, C.-C. Liu, K.-C. Wang, H.-P. Jhong, J.-F. Lee, C.-H. Wang, Journal of Materials Chemistry A 5 (2017) 19790-19799.
[27] K. Yuan, S. Sfaelou, M. Qiu, D. Lützenkirchen-Hecht, X. Zhuang, Y. Chen, C. Yuan, X. Feng, U. Scherf, ACS Energy Letters 3 (2018) 252-260.
[28] L. Qiheng, C. Wenxing, X. Hai, G. Yue, L. Zhi, Z. Lirong, Z. Xusheng, Y. Wensheng, C. Weng-Chon, S. Rongan, F. Ninghua, G. Lin, Z. Zhongbin, C. Chen, W. Dingsheng, P. Qing, L. Jun, L. Yadong, Adv Mater 0 (2018) 1800588.
[29] Y. Hu, J. Zhu, Q. Lv, C. Liu, Q. Li, W. Xing, Electrochim Acta 155 (2015) 335-340.
[30] M. Bruna, A.K. Ott, M. Ijäs, D. Yoon, U. Sassi, A.C. Ferrari, ACS Nano 8 (2014) 7432-7441.
[31] A.C. Ferrari, D.M. Basko, Nat. Nanotechnol. 8 (2013) 235-246.
[32] Y. Ito, W. Cong, T. Fujita, Z. Tang, M. Chen, Angew. Chem. In. Ed. 54 (2015) 2131-2136.
[33] D. Li, Y. Jia, G. Chang, J. Chen, H. Liu, J. Wang, Y. Hu, Y. Xia, D. Yang, X. Yao, Chem 4 (2018) 1-12.
[34] Z. Lu, J. Wang, S. Huang, Y. Hou, Y. Li, Y. Zhao, S. Mu, J. Zhang, Y. Zhao, Nano Energy 42 (2017) 334-340.
[35] X. Li, X. Huang, S. Xi, S. Miao, J. Ding, W. Cai, S. Liu, X. Yang, H. Yang, J. Gao, J. Wang, Y. Huang, T. Zhang, B. Liu, J Am Chem Soc 140 (2018) 12469-12475.
[36] K. Jiang, S. Siahrostami, T. Zheng, Y. Hu, S. Hwang, E. Stavitski, Y. Peng, J. Dynes, M. Gangisetty, D. Su, K. Attenkofer, H. Wang, Energy & Environmental Science 11 (2018) 893-903
[37] N. Ramaswamy, U. Tylus, Q. Jia, S. Mukerjee, J Am Chem Soc 135 (2013) 15443-15449.
[38] Q.-L. Zhu, W. Xia, L.R. Zheng, R. Zou, Z. Liu, Q. Xu, ACS Energy Letters 2 (2017) 504-511.
[39] W. Liu, L. Zhang, X. Liu, X. Liu, X. Yang, S. Miao, W. Wang, A. Wang, T. Zhang, J Am Chem Soc 139 (2017) 10790-10798.
[40] X. Wang, Z. Chen, X. Zhao, T. Yao, W. Chen, R. You, C. Zhao, G. Wu, J. Wang, W. Huang, J. Yang, X. Hong, S. Wei, Y. Wu, Y. Li, Angewandte Chemie International Edition 57 (2018) 1944-1948.

[41] Y. Mun, S. Lee, K. Kim, S. Kim, S. Lee, J.W. Han, J. Lee, J Am Chem Soc 141 (2019) 6254-6262.
[42] M. Asadi, B. Kumar, A. Behranginia, B.A. Rosen, A. Baskin, N. Repnin, D. Pisasale, P. Phillips, W. Zhu, R. Haasch, R.F. Klie, P. Král, J. Abiade, A. Salehi-Khojin, Nature Communications 5 (2014) 4470.
[43] W. Bi, X. Li, R. You, M. Chen, R. Yuan, W. Huang, X. Wu, W. Chu, C. Wu, Y. Xie, Adv Mater 30 (2018) 1706617.
[44] M. Ma, B.J. Trześniewski, J. Xie, W.A. Smith, Angewandte Chemie International Edition 55 (2016) 9748-9752.
[45] A. Wuttig, M. Yaguchi, K. Motobayashi, M. Osawa, Y. Surendranath, Proceedings of the National Academy of Sciences 113 (2016) E4585-E4593.
[46] Y. Jiao, Y. Zheng, K. Davey, S.-Z. Qiao, Nature Energy 1 (2016) 16130.
[47] F. Pan, B. Li, X. Xiang, G. Wang, Y. Li, ACS Catalysis 9 (2019) 2124-2133.
[48] H. Hu, B. Guan, B. Xia, X.W. Lou, J Am Chem Soc 137 (2015) 5590-5595.
[49] D.H. Won, H. Shin, J. Koh, J. Chung, H.S. Lee, H. Kim, S.I. Woo, Angewandte Chemie International Edition 55 (2016) 9297-9300.
[50] H. Zhang, S. Hwang, M. Wang, Z. Feng, S. Karakalos, L. Luo, Z. Qiao, X. Xie, C. Wang, D. Su, Y. Shao, G. Wu, J Am Chem Soc 139 (2017) 14143-14149.
[51] F. Pan, H. Zhang, K. Liu, D.A. Cullen, K.L. More, M. Wang, Z. Feng, G. Wang, G. Wu, Y. Li, ACS Catalysis 8 (2018) 3116-3122.
[52] Y. Zheng, Y. Jiao, L.H. Li, T. Xing, Y. Chen, M. Jaroniec, S.Z. Qiao, ACS Nano 8 (2014) 5290-5296.
[53] R. Paul, F. Du, L. Dai, Y. Ding, Z.L. Wang, F. Wei, A. Roy, Adv Mater 31 (2019) 1805598.
[54] Y. Chen, S. Ji, S. Zhao, W. Chen, J. Dong, W.-C. Cheong, R. Shen, X. Wen, L. Zheng, A.I. Rykov, S. Cai, H. Tang, Z. Zhuang, C. Chen, Q. Peng, D. Wang, Y. Li, Nature Communications 9 (2018) 5422.
[55] Z. Geng, X. Kong, W. Chen, H. Su, Y. Liu, F. Cai, G. Wang, J. Zeng, Angewandte Chemie International Edition 57 (2018) 6054-6059.
[56] J.K. Nørskov, J. Rossmeisl, A. Logadottir, L. Lindqvist, J.R. Kitchin, T. Bligaard, H. Jónsson, J. Phys. Chem. B. 108 (2004) 17886-17892.